PAPER

Effects of proton irradiation on structural and electrochemical charge storage properties of TiO₂ nanotube electrodes for lithium-ion batteries†

Kassiopeia A. Smith,[a] Andreas I. Savva,[a] Changjian Deng,[a] Janelle P. Wharry,[b] Sooyeon Hwang,[c] Dong Su,[c] Yongqiang Wang,[d] Jue Gong,[e] Tao Xu,[e] Darryl P. Butt[f] and Hui Xiong [ID] *[a]

The effects of proton irradiation on nanostructured metal oxides have been investigated. Recent studies suggest that the presence of structural defects (*e.g.* vacancies and interstitials) in metal oxides may enhance the material's electrochemical charge storage capacity. A new approach to introduce defects in electrode materials is to use ion irradiation as it can produce a supersaturation of point defects in the target material. In this work we report the effect of low-energy proton irradiation on amorphous TiO₂ nanotube electrodes at both room temperature and high temperature (250 °C). Upon room temperature irradiation the nanotubes demonstrate an irradiation-induced phase transformation to a mixture of amorphous, anatase, and rutile domains while showing a 35% reduction in capacity compared to anatase TiO₂. On the other hand, the high temperature proton irradiation induced a disordered rutile phase within the nanotubes as characterized by Raman spectroscopy and transmission electron microscopy, which displays an improved capacity by 20% at ∼240 mA h g⁻¹ as well as improved rate capability compared to an unirradiated anatase sample. Voltammetric sweep data were used to determine the contributions from diffusion-limited intercalation and capacitive processes and it was found that the electrodes after irradiation had more contributions from diffusion in lithium charge storage. Our work suggests that tailoring the defect generation through ion irradiation within metal oxide electrodes could present a new avenue for designing advanced electrode materials.

Introduction

Titanium-based oxide materials have attracted intense attention as promising anode materials for Li-ion batteries due to their excellent cycling stability, low cost, abundance and environmentally benign nature.[1–4] Ti-based oxide materials are one of the few metal oxide materials that intercalate Li ions at relatively low voltages as anodes (∼1.5–1.8 V *vs.* Li/Li⁺) for a decent output voltage between cathodes and have been found as a safe alternative to the graphite anode. In addition, TiO₂ has a comparable theoretical specific capacity of 335 mA h g⁻¹ or 1.0 Li per TiO₂, compared to graphite (theoretical capacity: 372

mA h g⁻¹). The cycling stability of TiO₂ is superior compared to other conversion-type metal oxide anodes such as iron oxide. Among various TiO₂ polymorphs investigated for their electrochemical properties, researchers have found that rutile (space group *P*4₂/*mnm*), anatase (*I*4₁/*amd*), brookite (*Pbca*) and TiO₂-B (*C*2/*m*) show lithium electrochemical reactivity. The first attempts at using TiO₂ as a durable and safe electrode material focused on microcrystalline TiO₂ materials such as rutile, anatase and TiO₂-B.[5] These electrodes showed moderate specific capacities (the maximum Li uptake of 0.5 Li/Ti for anatase and TiO₂-B, and no activity for rutile)[5] due to the limited room temperature reactivity and conductivity on the microscale. Such limitations in room temperature reactivity of bulk TiO₂ have spurred rapid development in nanostructured TiO₂ materials, leading to significant improvements in electrochemical properties.[2,6–13] Nanosizing of TiO₂ has significantly improved the electrochemical reactivity toward Li at room temperature due to enhanced kinetics.[2,6–16] Upon lithium insertion, the donated charge is distributed between the Ti and O ions, leading to structural deformation. The existence of interstitial sites or vacancies within the structure may play an important role in atomic rearrangement to achieve the most thermodynamically stable phase with improved charge storage

[a] Micron School of Materials Science and Engineering, Boise State University, Boise ID 83725, USA. E-mail: ClaireXiong@BoiseState.edu; Tel: +1 208 426-5671

[b] School of Nuclear Engineering, Purdue University, West Lafayette, IN 47907, USA

[c] Center for Functional Materials, Brookhaven National Laboratory, Upton, NY, USA

[d] Ion Beam Materials Laboratory, Los Alamos National Laboratory, Los Alamos, NM, USA

[e] Department of Chemistry & Biochemistry, Northern Illinois University, Dekab, IL, USA

[f] College of Mines and Earth Sciences, University of Utah, Salt Lake City, Utah, USA

† Electronic supplementary information (ESI) available. See DOI: 10.1039/c7ta01026e

This journal is © The Royal Society of Chemistry 2017

J. Mater. Chem. A, 2017, 5, 11815–11824 | 11815

capacity. Recent studies have investigated enhanced electro-chemical charge storage in electrodes that contain intentional structural defects (*e.g.* vacancies and interstitials).[17–19] Our recent studies, along with studies by others, have suggested that nanoscale transition metal oxides, which have structural defects with local disorder, can offer enhanced capacity and structural stability under stress.[17,20–25] Further, researchers have demonstrated that synthetic methods such as doping[17,26] and ion irradiation[17,26–35] can introduce defects that could enhance the charge storage of metal oxides. A new approach to introduce defects in electrode materials is to utilize irradiation to produce a supersaturation of defects in the target material.[36]

It is widely recognized that ion irradiation, *i.e.* the bombardment of a target with keV to MeV ions, introduces defects and regions of lattice disorder in solids.[36] Furthermore, electron and light ion irradiation (*e.g.* proton) have been shown by molecular dynamics to predominantly produce point defects in rutile and anatase TiO_2.[37,38] Through these theoretical studies, it was found that grain boundaries in both polymorphs behave as sinks for all types of point defects.[37] From this, it may be inferred that nanostructured materials could have a high radiation resistance owing to their large volume fraction of grain boundaries. Nevertheless, the defect properties and the defect dynamics are largely unknown in irradiated nano-structured TiO_2 materials. The nature of structural changes upon irradiation also depends on the incoming ion species. Hartmann *et al.*[39] observed amorphization of single crystal rutile TiO_2 at room temperature when irradiated with He^+ ions, but found that temperatures under 200 K were necessary to amorphize the same materials under heavy noble gas ions. It was suggested that He^+ ions create a number of small cascades which allow point defects to accumulate in the target material.

In the present work, we investigated the effect of proton irradiation both at room temperature and at an elevated temperature on amorphous TiO_2 nanotube (TiO_2-NT) electrodes. TiO_2 has been widely studied as an anode material for Li-ion batteries. However, to the best of authors' knowledge no work has been carried out to study the electrochemical charge storage properties of ion-irradiated nanostructured TiO_2. In addition, no work has been carried out to investigate the ion irradiation effect on nanoscale amorphous ceramics. Recently Schmuki *et al.* explored proton irradiation induced defects of anatase TiO_2-NT films for photocatalytic H_2 evolution.[40] It was shown that proton implantation into anatase TiO_2-NTs induced specific defects and created intrinsic co-catalytic centers for improved photocatalytic activity. Hence, proton irradiation could be an effective tool for defect-driven materials with enhanced functionality.

In this work, we conducted proton implantation at an energy of 200 keV with an average dose of 0.17 displacements per atom (dpa) on amorphous TiO_2-NT electrodes both at room temperature and at 250 °C. Structural characterization by Raman spectroscopy and transmission electron microscopy (TEM) suggests that proton irradiation induces phase transformation in the amorphous TiO_2-NT electrode. For the sample irradiated at room temperature (RT), irradiation-induced phase transformation to a mixture of disordered anatase and rutile phases

was observed. On the other hand, for the sample irradiated at 250 °C (HT), we observed a phase transformation to a primarily disordered rutile phase. It is interesting to note that no work has been carried out for the synthesis of rutile TiO_2-NTs prepared by anodization. In general, anatase TiO_2-NTs can be prepared by thermally annealing the as-prepared amorphous TiO_2-NTs at temperatures around 450 °C.[41] However, the same thermal treatment is not viable to synthesize rutile TiO_2-NTs as the tubes tend to collapse at the phase transition temperature for rutile (>600 °C). Therefore, the proton implantation approach might open a new synthetic pathway for creating anodized rutile TiO_2-NTs. We have also conducted electrochemical characterization of the irradiated TiO_2-NT electrodes, where we observe the charge storage behavior of the TiO_2-NT electrode change. Galvanostatic intermittent titration technique (GITT) measurements were conducted and it was found that the sample irradiated at 250 °C exhibits enhanced diffusion compared to the RT sample. The sample irradiated at 250 °C also demonstrates improved capacity at a low rate and superior rate capability compared to both the RT irradiated sample and the anatase TiO_2-NTs. Our results suggest that by tailoring the irradiation conditions it is possible to create nanostructured metal oxide electrodes with enhanced functionality.

Results & discussion

Densely packed, vertically oriented TiO_2-NTs were synthesized by an electrochemical anodization method described previously.[24] TiO_2-NTs are inherently connected to the Ti substrate – the current collector – eliminating the need for conductive carbon additives and polymer binders which are typically used in electrodes for lithium-ion batteries. The SEM top-view image in Fig. 1a shows the TiO_2-NT after the anodization. The as-prepared TiO_2-NT film is ~1 μm in length (ESI Fig. S1†) and has an outer diameter of ~60 nm with a ~10 nm wall thickness. The stability of the TiO_2-NT morphology after proton irradiation was investigated by SEM. Fig. 1b shows the top-view SEM image of the TiO_2-NT film after proton irradiation at room temperature, exhibiting the structural integrity of the nanotubes after irradiation. The inset of Fig. 1b shows a representative TEM image of the tube morphology after irradiation, showing no degradation.
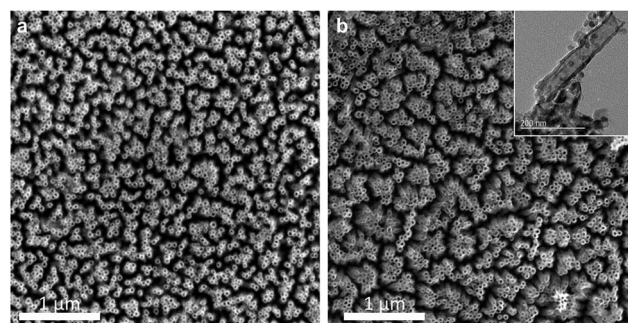

Fig. 1 (a) SEM top view of a TiO_2-NT film before irradiation and (b) after irradiation (inset: TEM image of the tube after irradiation).

11816 | *J. Mater. Chem. A*, 2017, **5**, 11815–11824

This journal is © The Royal Society of Chemistry 2017

TiO$_2$-NT films were ion implanted with protons (p$^+$) at an energy of 200 keV with a fluence of 2.18×10^{17} ions per cm^2 to achieve the average accumulated proton dose of 0.17 dpa. For these experiments, implantations were carried out either at room temperature or at 250 °C. Fig. 2 shows the damage depth distribution for compact TiO$_2$ according to Monte Carlo simulations using SRIM 2013.[42] In these calculations, the implantation leads to an implant zone reaching approximately 1.3 μm below the sample surface with a maximum of p$^+$ implanted at a depth of 1.25 μm. The simulation is performed based on compact or bulk materials, and it has been suggested by Schmuki *et al.* that the actual damage depth in TiO$_2$-NT films may be greater due to the porosity of the film.[40] The nanotube length was chosen such that there is minimum variation in irradiation along the full length of the tube, *i.e.*, the tube length is less than the depth of the damage peak.

The as-prepared, irradiated and anatase TiO$_2$-NT samples were evaluated using Raman spectroscopy for their phase composition as well as the degree of order–disorder in a short range (Fig. 3). Raman spectroscopy is a powerful tool used to investigate the structure and order–disorder of TiO$_2$ and its polymorphs.[43–49] Anatase TiO$_2$ has a tetragonal structure (space group $I4_1/amd$) and is comprised of two TiO$_2$ units per primitive cell, leading to six Raman active modes in the vibrational spectrum: three E$_g$ modes centered around 144, 196, and 639 cm^{-1} (designated as E$_{g(1)}$, E$_{g(2)}$ and E$_{g(3)}$ here, respectively), two B$_{1g}$ modes centered around 397 and 519 cm^{-1} (designated as B$_{1g(1)}$, and B$_{1g(2)}$ here, respectively), and an A$_{1g}$ mode at 513 cm^{-1}. Due to the overlapping of B$_{1g(2)}$ and A$_{1g}$ modes the symmetry assignment of the two modes has been difficult. On the other hand, rutile TiO$_2$ (space group $P4_2/mnm$) has only four Raman active modes: B$_{1g}$ (143 cm^{-1}), E$_g$ (447 cm^{-1}), A$_{1g}$ (612 cm^{-1}), and B$_{2g}$ (826 cm^{-1}). The rutile spectra also exhibit several broad combination bands exhibited around 250 cm^{-1}, 360 cm^{-1}, 550 cm^{-1}, and 680 cm^{-1}.[50,51] Note that the E$_{g(1)}$ mode of anatase and B$_{1g}$ mode of rutile appear around the same frequency. Consequently in a two-phase sample, the 144 cm^{-1} peak can have the contribution from both modes.
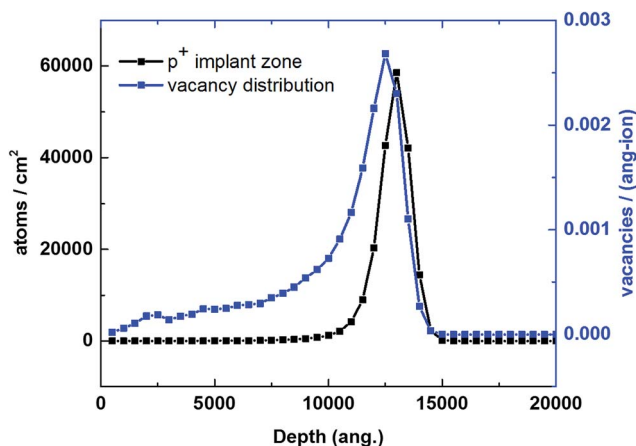

Fig. 2 Depth distribution calculation of implanted ions (H ions) and the resulting damage profile (Ti-, O-recoil) for anatase TiO$_2$.
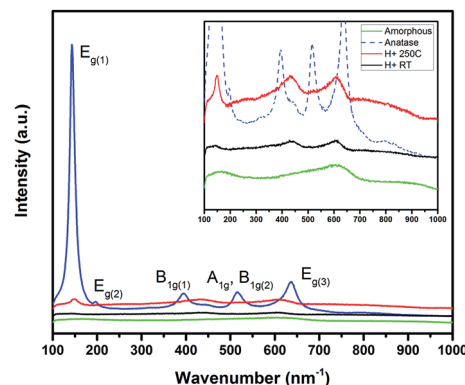

Fig. 3 Raman spectra of unirradiated anatase TiO$_2$ nanotubes (blue), unirradiated amorphous nanotubes (green), HT-TiO$_2$ proton irradiated nanotubes (red), and RT-TiO$_2$ proton irradiated nanotubes (black). Inset shows the zoomed-in view.

Fig. 3 shows the Raman spectra of unirradiated anatase, the as-prepared amorphous and the irradiated TiO$_2$-NT samples. The broad Raman spectrum of the as-prepared TiO$_2$-NT is indicative of its amorphous nature, which contains a variety of phonon scattering centers. In the unirradiated anatase control sample, five well-defined peaks are observed at around 143.3, 196.5, 395, 514.5, and 637.2 cm^{-1}, corresponding to the vibration modes of the anatase phase. The presence of well-defined, high intensity peaks in the pristine anatase TiO$_2$-NT suggests a high order of crystallinity with little disorder.

In Raman spectroscopy, the phonon confinement model links the q vector selection rule for the excitation of Raman active phonons with the degree of ordering and crystallite size.[48,49,51] In a perfect crystal with a long-range order, there would be phonon conservation so that only the optic zones near the Brillouin zone (BZ) center are observable, allowing for sharp and well defined peaks. However, when a material lacks a long range order, or in this case is nanocrystalline, the selection rule is relaxed resulting in peak broadening and possible shifts as a result of the increased range of q vectors.[50–53] In first-order Raman scattering, the modification of the Raman line shape for a given phonon mode as a function of crystallite size is determined by the behavior of the dispersion slope away from the BZ center (scattering vector $q \approx 0$). A negative slope would cause a red-shifted Raman peak, while a positive slope would result in a blue-shifted Raman peak, in addition to asymmetric peak broadening when the crystallite size is reduced.[48]

Upon proton irradiation, both the HT and RT samples show an increase in crystallinity from the original amorphous state. The peaks present after irradiation are broad compared to a purely crystalline structure, indicating a disordered lattice.[45] In anatase TiO$_2$ nanocrystals, it has been found that B$_{1g(1)}$ (396 cm^{-1}) and E$_{g(3)}$ (639 cm^{-1}) modes are the most sensitive to the presence of defects compared to the most intense E$_{g(1)}$ (144 cm^{-1}) mode.[45] In the sample irradiated at room temperature (TiO$_2$-NTs (RT)), the E$_{g(1)}$ and the E$_{g(3)}$ peaks of the anatase structure are observable but weak due to the lack of a long range order. Two broad peaks are present at 435.4 and 607.5 cm^{-1}.

This journal is © The Royal Society of Chemistry 2017

J. Mater. Chem. A, 2017, 5, 11815–11824 | **11817**

The peak at 435.4 cm^{-1} can have contribution from both the B$_{1g(1)}$ mode in anatase and E$_g$ mode in the new rutile phase. The peak at 607.5 cm^{-1} is assigned to the A$_{1g}$ mode of the new rutile phase. We have also observed the phase transformation in the TEM study, which will be discussed later. It is well known that irradiation can create point defects (vacancies and interstitials) in materials. This result suggests an irradiation-assisted phase transformation from amorphous to anatase and rutile, which is consistent with observations of thermal spike-induced nano-phase transformations in localized regions within ion tracks in ceramic materials.[54–57] Because these irradiation-assisted phase transformations are by nature highly localized and nanoscopic, in contrast to a bulk annealing-induced phase transformation, a combination of disordered and ordered phases can be found.

For the irradiated sample at 250 °C (TiO$_2$-NTs (HT)), there is a distinct peak at 148.9 cm^{-1}, which can be ascribed to either the anatase or rutile phase. The full width at half maximum (FWHM) of the peak is 20 cm^{-1} and is broader than the FWHM of the E$_{g(1)}$ peak of the pure anatase TiO$_2$ sample. The strongest rutile vibrational mode A$_{1g}$[50] is present at 607 cm^{-1} and is more defined in the TiO$_2$-NT (HT) sample compared to that in the TiO$_2$-NT (RT) sample. In fact, the overall spectrum begins to more closely resemble the rutile structure including several rutile combinational bands which are centered at approximately 250, 350, 540, and 680 cm^{-1}.[50] Much like the room temperature irradiation case, these results can also be explained by thermal spikes from ion irradiation. However, the higher irradiation temperature, in combination with the thermal spikes, can more effectively provide sufficient thermal energy to induce the rutile phase transformation. It should be noted that no result on rutile TiO$_2$ nanotubes formed by anodization has been reported and the proton irradiation at
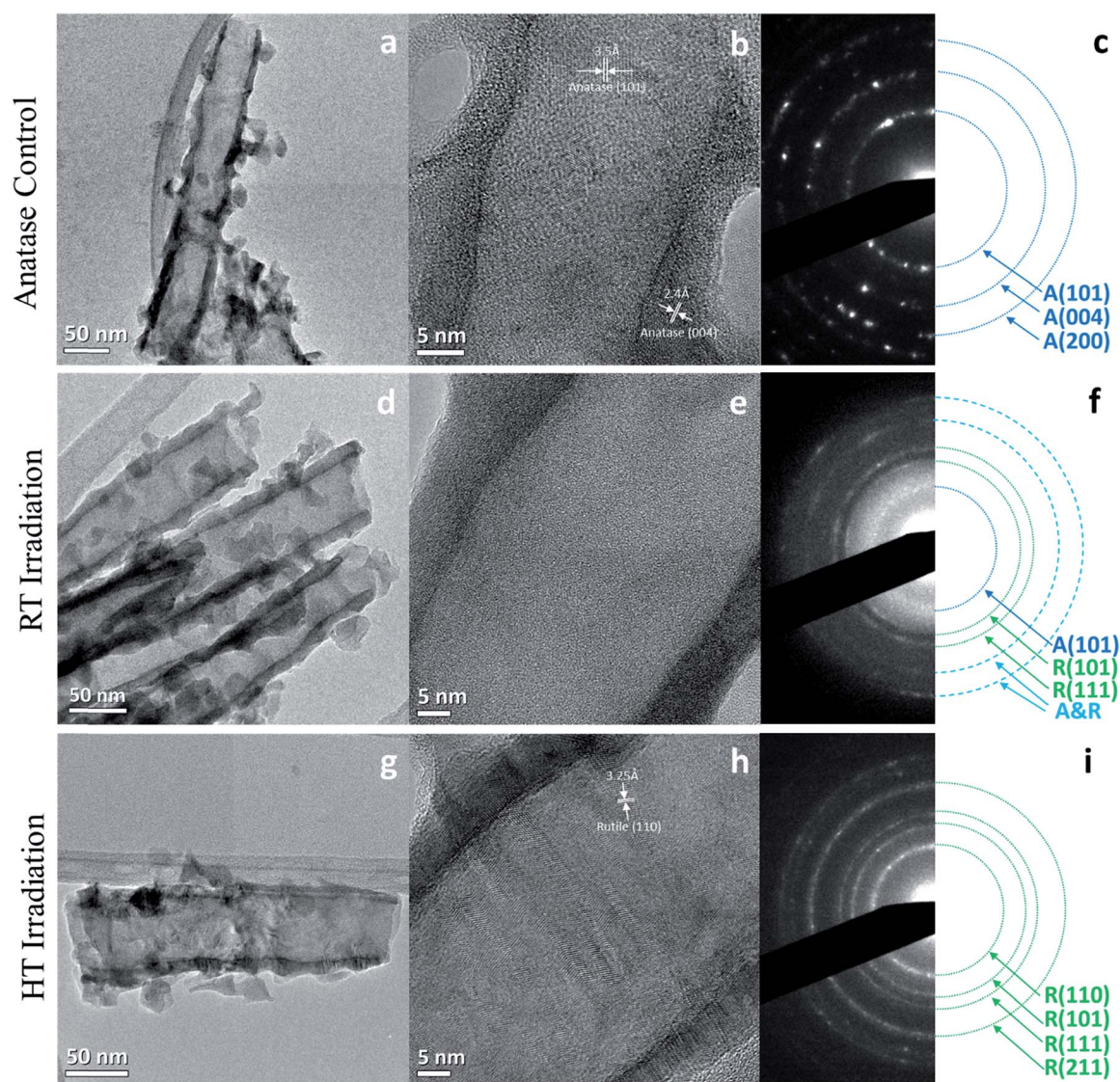

Fig. 4 Low magnification TEM (a, d, and g) of unirradiated anatase TiO$_2$ nanotubes, RT proton irradiated nanotubes, and HT irradiated nanotubes, respectively, showing the retained structural morphology after irradiation. HRTEM images of the unirradiated anatase TiO$_2$ nanotubes, RT proton irradiated nanotubes, and HT irradiated nanotubes (b, e, and h, respectively), and their corresponding SAED patterns (c, f, and i, respectively).

higher temperature could open a new avenue for rutile nanotube synthesis.

In both cases after irradiation the peaks are broad and have low intensities suggesting the presence of disordered anatase and rutile phases.[45,49]

We also evaluated the electrical conductivities of the pristine anatase and irradiated TiO_2-NT samples using a two-point conductivity measurement.[58] There is no significant difference between the unirradiated amorphous and irradiated TiO_2-NT samples and their conductivities are significantly lower (~2 orders of magnitude) than that of the unirradiated anatase sample. The results indicate that although irradiation can increase the carrier density[40], the carrier mobility is not necessarily increased; therefore an increase in electrical conductivity is not observed in irradiated samples.

TEM was used to study the phase evolution of proton irradiated TiO_2-NT samples. Low magnification (4a, d and g), high resolution TEM (HRTEM) (4b, e and h) and SAED pattern (4c, f and i) images of the unirradiated anatase and proton implanted nanotubes are shown in Fig. 4. The low magnification images show that even after irradiation, the overall tube structure is well maintained and there is no evidence of failure in their structural integrity. Since TiO_2 NT samples were acquired by scraping them from the substrate for TEM observation, their full length is not observed under this technique. Fig. 4b shows that the anatase sample is composed of randomly oriented nanocrystals, which have an anatase structure according to SAED patterns shown in Fig. 4c. After irradiation at RT, the HRTEM image shows that there is no long-range order in the RT sample and it still appears predominantly amorphous (Fig. 4e). The SAED pattern of the TiO_2-NT (RT) sample (Fig. 4f) shows faint rings originating from both anatase and rutile structures, implying that the amorphous structure of TiO_2 has transformed to a partially crystalline structure with short-range-ordered anatase and rutile phases after irradiation at RT. On the other hand, proton implantation at high temperature leads to the phase transformation to rutile as presented by the SAED pattern (Fig. 4i). The HRTEM image shows that the NT sample has a crystalline phase with a number of defects. In other words, phase transformation to rutile is accompanied with evolution of defects within NT samples during irradiation at high temperature.

Structural and chemical properties of TiO_2-NTs before and after proton implantation are further characterized by electron energy loss spectroscopy (EELS) (Fig. 5). The Ti $L_{2,3}$ edge of crystalline TiO_2 is composed of well-separated L_3 and L_2 edges, which originated from the 2p core-hole spin–orbit coupling. Each L_3 and L_2 edge is also divided into two edges by strong crystal-field splitting.[59] Clear crystal-field splitting in the L_3 and L_2 edges of anatase and HT irradiated samples demonstrates that these samples have a similar chemical state of Ti^{4+} while the different feature of the oxygen K-edge is originated from the different crystal structure.[60] The strong prepeak splitting in the oxygen K-edge spectra of the HT and anatase samples is due to the Ti 3d–O 2p hybridization split by the local octahedral crystal field.[59,60] The three-peak feature near 540 eV in the HT sample resembles the oxygen 2p–Ti 4s and 4p hybridization of the rutile

phase.[60] After proton implantation at RT, crystal-field splitting in the Ti $L_{2,3}$ edge is indistinct, which reflects the presence of an amorphous phase.[61]

Fig. 6 compares the charge/discharge profiles of the irradiated and control TiO_2 samples cycled between 0.9 and 2.5 V (vs. Li/Li^+) at a low current rate. Lithium insertion in electrode materials can proceed via a two-phase structural transition or single-phase solid solution charge storage behavior. The voltage profile (Fig. 6) accounts for the structural behavior during lithium insertion/extraction. Anatase TiO_2 exhibits a two-phase region which occurs at the characteristic plateau of approximately 1.7 V vs. Li/Li^+, indicating the coexistence of a Li-poor phase $Li_{0.05}TiO_2$, which maintains the original anatase structure (space group: $I4_1/amd$) and a Li-rich phase $Li_{0.5}TiO_2$ (space group: $Imma$).[62]

After irradiation, both the HT and RT samples display sloping curves, indicating single-phase solid solution behavior. The RT sample consists of a mixture of anatase, rutile, and amorphous regions, which could impede the diffusion of Li ions. This may explain why it has the lowest capacity (~130 mA h g^{-1}) among the three. The HT sample displays the highest capacity (~240 mA h g^{-1}) of the three, suggesting enhanced lithium charge storage of the disordered rutile nanotubes after irradiation at 250 °C (Fig. 7). The capacities of all three samples are quite reversible after 20 cycles at low current rates. It was noted that the coulombic efficiency of both irradiated samples in the initial cycle is much lower (~40–42%) than that of the unirradiated anatase sample (~78%). The low coulombic efficiency could be ascribed to the defects induced by proton irradiation, which are highly reactive with the electrolyte and could lead to more side reactions.
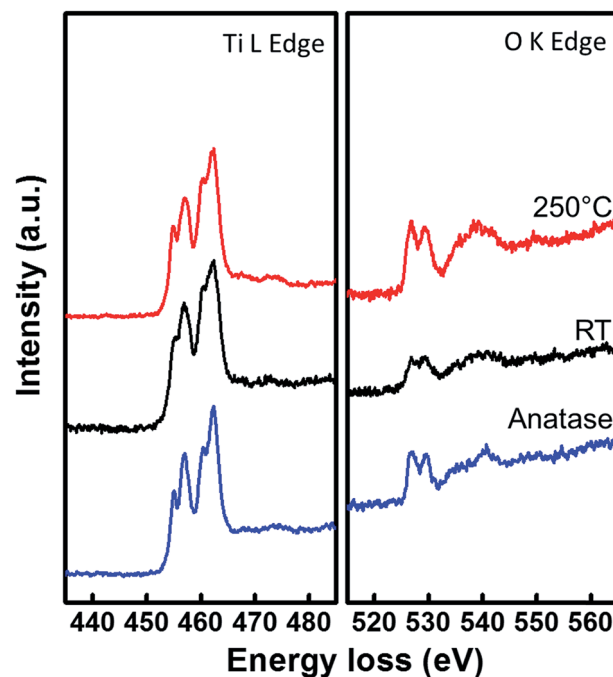

Fig. 5 Electronic energy loss spectra (EELS) of the unirradiated anatase TiO_2, RT proton irradiated TiO_2 and HT proton irradiated TiO_2 nanotube samples.

This journal is © The Royal Society of Chemistry 2017

J. Mater. Chem. A, 2017, 5, 11815–11824 | 11819

The rate capability study (Fig. 8) confirms the superior diffusion of Li ions in the HT sample compared to those in both the RT sample and the unirradiated anatase samples. This is especially apparent at the highest rate, where the HT irradiated sample exhibits a reversible capacity of 130 mA h g^{-1} when cycled at 2 A g^{-1}, whereas the anatase sample has a capacity of approximately 85 mA h g^{-1} when cycled at 1 A g^{-1}. The RT sample also exhibits lower performance of only 20 mA h g^{-1} but at a higher current density of 4 A g^{-1}. From the GITT analysis (ESI Fig. S2†), the HT irradiated TiO$_2$ exhibits a range of Li$^+$ diffusivity of ~1 × 10^{-13} to ~2 × 10^{-14} cm^2 s^{-1} during Li insertion from 2–1 V, whereas the RT irradiated TiO$_2$ exhibits an inferior Li$^+$ diffusivity of ~3 × 10^{-14} to 4 × 10^{-15} cm^2 s^{-1} in the same range. This result corroborates well with results from the rate capability study. In addition, the Li$^+$ diffusivity of the disordered rutile HT sample is between that of the Li diffusion along the c-axis (10^{-6} cm^2 s^{-1}) and that of the ab-plane (10^{-15} cm^2 s^{-1}),[2,63] suggesting that the unique disordered rutile structure of the HT sample may unblock Li$^+$ diffusion pathways which were previously restricted by the rigid crystalline structure.

The lithium storage mechanism was investigated by sweep cyclic voltammetry (Fig. 9 and ESI S3†). A pair of redox peaks (Fig. 9b) at ~1.7 V in cathodic scan and 2.15 V in anodic scan was observed in the unirradiated anatase TiO$_2$-NT sample, which is consistent with previous studies.[64] However, the peaks become broader and indistinct in the voltammograms of both irradiated samples. Furthermore, the capacitive and diffusion contributions to electrochemical charge storage in TiO$_2$ of each sample were analyzed with varying scan rates according to the following equation:[65]

$$i = av^b \qquad (1)$$

where the measured current i obeys a power law relationship with scan rate v. Both a and b are adjustable parameters. The b value can be determined by plotting log(i) $versus$ log(v). A b value of 0.5 indicates that the process is limited by diffusion according to the following equation:[66]

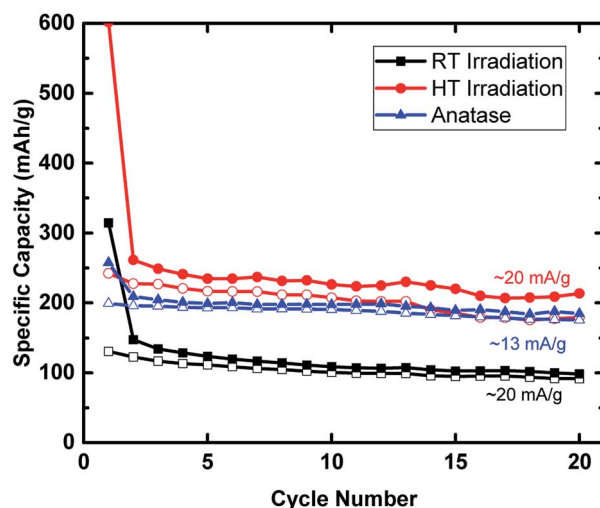$$i = nFAC^*D^{1/2}v^{1/2}\left(\frac{\alpha nF}{RT}\right)^{1/2}\pi^{1/2}\chi(bt) \qquad (2)$$

Fig. 7 Low rate galvanostatic cycling of unirradiated anatase nanotubes (blue), RT proton irradiated nanotubes (black), and HT proton irradiated nanotubes (red) between 0.9 and 2.5 V vs. Li/Li$^+$. Solid symbols: discharge capacities. Hollow symbols: charge capacities.

where n is the number of electrons involved in the electrode reaction, F is the Faraday constant, A is the surface area of the electrode material, C^* is the surface concentration, D is the diffusion coefficient, R is the gas constant, α is the transfer coefficient, T is the temperature, and $\chi(bt)$ is the normalized current for a totally irreversible system in cyclic voltammetry. A current response following eqn (2) is indicative of a diffusion-controlled faradaic intercalation process.[64,67] On the other hand, $b = 1$ suggests that the charge storage is dominated by a capacitive process where the current is correlated with the capacitance according to the following equation:[65]

$$i_c = vC_dA \qquad (3)$$

where C_d is the capacitance. For unirradiated anatase TiO$_2$-NT electrodes, at a peak potential of 1.7 V the b-value is 0.55, which indicates that the process is primarily a diffusion-limited intercalation reaction and is consistent with the previous work.[64] At potentials higher or lower than the peak potential, the
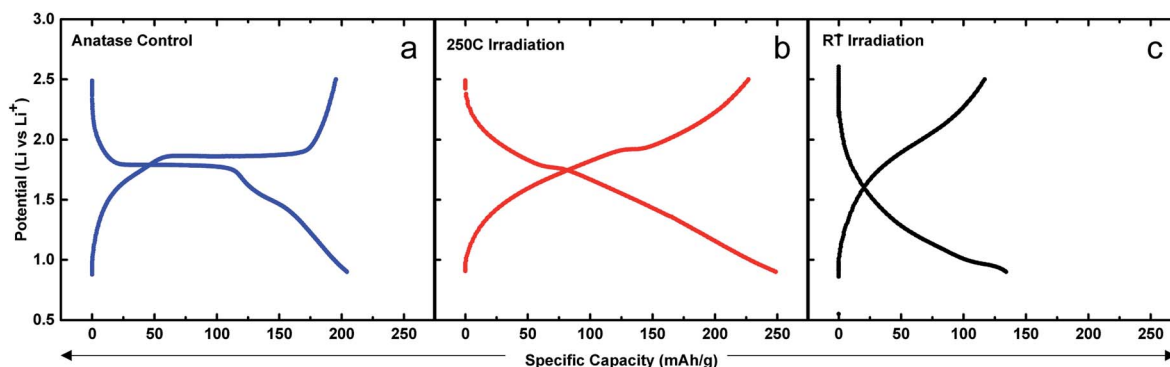

Fig. 6 Charge/discharge curves of the unirradiated anatase nanotube anode (a), the HT proton irradiated TiO$_2$ nanotubes (b), and the RT proton irradiated TiO$_2$ nanotubes (c).
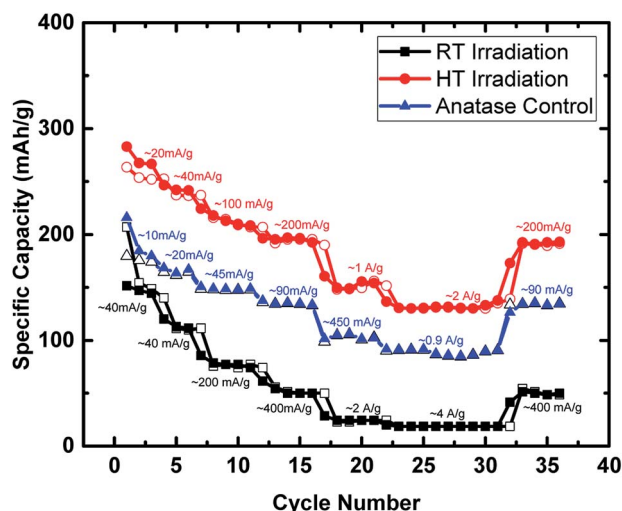
Fig. 8 Galvanostatic rate study of unirradiated anatase nanotubes (blue), RT proton irradiated nanotubes (black), and HT proton irradiated nanotubes (red) between 0.9 and 2.5 V vs. Li/Li$^+$. Solid symbols: discharge capacities. Hollow symbols: charge capacities.

b-values are in the range of 0.7–0.9, indicating that the capacitive process becomes dominant. For the irradiated HT TiO$_2$-NT electrode, the b-values are fairly constant at around 0.7, which suggests that the lithium charge storage is controlled by both diffusion and capacitive processes. The b-values of irradiated RT TiO$_2$-NT electrodes are lower than those of the HT sample and are centered at 0.6, which indicate that the charge storage in RT electrodes is dominated by diffusion-limited intercalation. The mixed amorphous and crystalline domains in this material may hinder the lithium diffusion, which explains the inferior rate capability of the electrode.

The capacitive contribution in the electrode can be estimated through the following analysis:[64]

$$i(V) = k_1 v + k_2 v^{1/2} \qquad (4)$$

where the current response $i(V)$ is a combination of capacitor-like and diffusion controlled behaviors.[64] k_1v and $k_2v^{1/2}$ correspond to the capacitive and diffusion-controlled contribution,[64] respectively. By determining k_1 and k_2 through linear fitting of $i(V)/v^{1/2}$ versus $v^{1/2}$ as a function of potential, it is possible to calculate the contributions from diffusion-controlled intercalation and capacitor-like processes. The capacitive contribution
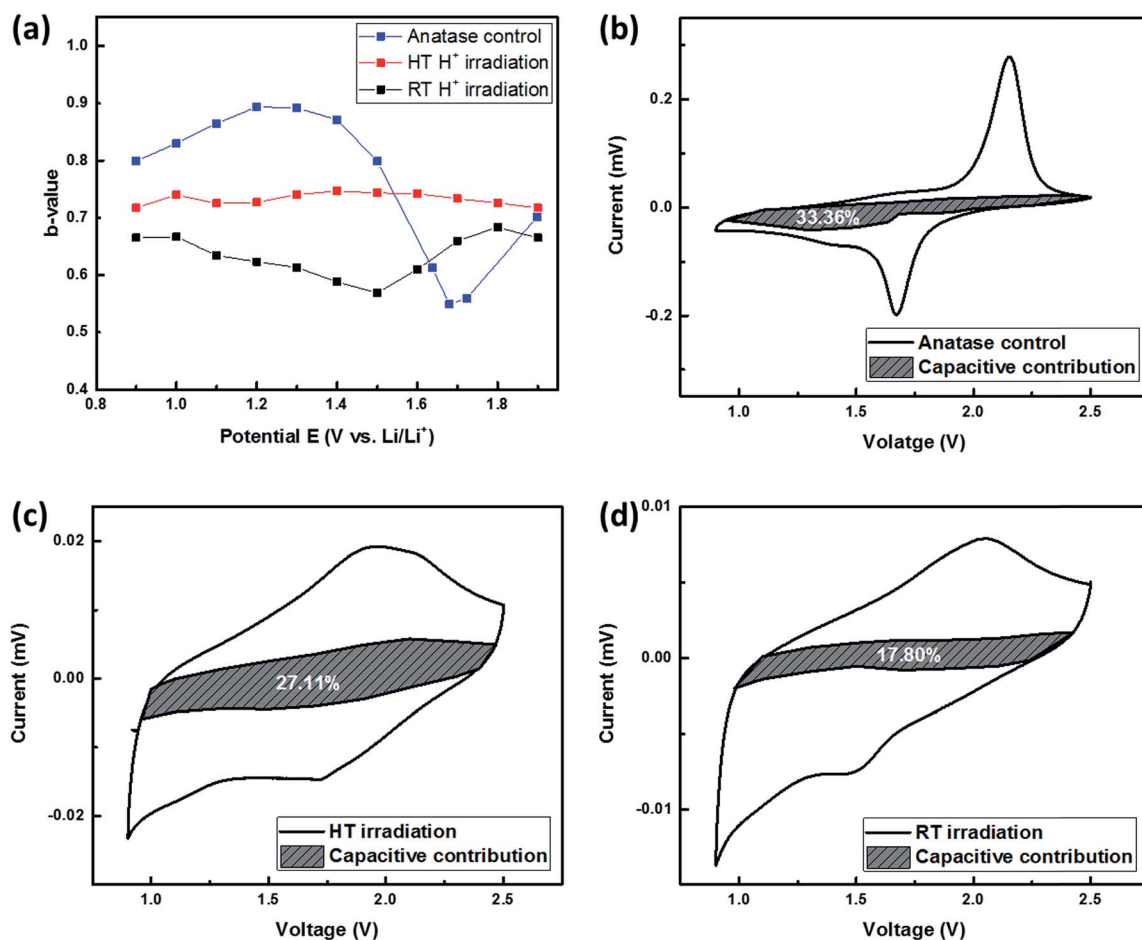

Fig. 9 (a) b-values and voltammetric response (0.5 mV s^{-1}) for (b) unirradiated anatase TiO$_2$-NTs, (c) HT proton irradiated TiO$_2$-NTs and (d) RT proton irradiated TiO$_2$-NTs. The capacitive currents (shaded region) are determined from the data in ESI Fig. S3.†

This journal is © The Royal Society of Chemistry 2017

J. Mater. Chem. A, 2017, 5, 11815–11824 | 11821

for unirradiated anatase, HT proton irradiated, and RT proton irradiated nanotubes was 33.36%, 27.11% and 17.80%, respectively. The results suggest that after irradiation there is more contribution from diffusion-limited intercalation to the lithium charge storage and there is a wide site energy distribution caused by the defects induced through proton irradiation, which correspond to the sloping characteristics of the voltage profiles of irradiated samples.

Conclusions

In summary, phase transformations were observed in amorphous TiO_2-NTs upon proton irradiation at both room temperature and high temperature. After 200 keV proton irradiation, TiO_2 nanotubes maintain their structural integrity and do not appear to undergo morphological degradation. The results from Raman spectroscopy and TEM indicate that for the sample under room temperature proton implantation, short-range-ordered crystallites were observed and the final structure is a mixture of anatase, amorphous and rutile domains. Under high temperature proton implantation, the nanotubes undergo a phase transformation from amorphous to a primarily disordered rutile phase. Both irradiated samples exhibit lithium charge storage behavior following a single-phase solid solution mechanism. The RT irradiated sample has a reduced capacity possibly due to the combination of anatase, rutile and amorphous phases present resulting in a reduced ion mobility. On the other hand, in the HT irradiated sample the capacity is improved, due to the disordered rutile structure. GITT results suggest that Li^+ diffusivity in the HT irradiated sample is higher than that of the RT irradiated sample, which is further confirmed by the enhanced rate capability of the HT irradiated sample. Analysis on the capacitive and diffusion contribution in lithium charge storage of irradiated TiO_2-NTs suggests that there is more contribution from diffusion-limited intercalation after irradiation. Our study presents a new pathway for designing new functional electrode materials with enhanced electrochemical charge storage properties through tailoring the ion irradiation conditions.

Experimental

Materials

TiO_2 nanotubes were synthesized by electrochemical anodization described previously.[24,68] To summarize, pure titanium foil (0.0127 mm, 99.8%, Alfa Aesar) was cleaned by a three step sonication in acetone, isopropyl alcohol and D.I. water before anodization. The back of the Ti foil was protected by tape to ensure uniform current distribution. Anodization was carried out in a two-electrode cell with a Pt mesh as the counter electrode. Anodization was carried out for 10 minutes under a constant voltage of 15 V in an electrolyte of 0.36 M ammonium fluoride (Aldrich) in 95 vol% formamide (Fisher) and 5 vol% DI water. The anodized samples were then ultrasonically cleaned with DI water for 30 seconds. Anatase TiO_2 was prepared by annealing the as-prepared TiO_2 NTs in a mixture of ultra-pure 20% O_2/balance Ar gas at 450 °C for 4 hours.

Irradiation

The TiO_2-NT films were irradiated with 200 keV protons in a 200 kV Varian ion implanter at Los Alamos National Laboratory. The accelerator beam line was maintained at 1.8×10^{-7} torr throughout the experiment. Specimens were mounted onto a copper irradiation stage, which was electrically isolated from the accelerator beam line, to allow for accurate charge collection. Thermocouples were mounted onto the copper stage and used to control the temperatures throughout the implantation. During irradiation, the focused proton beam was raster-scanned across samples, with the resulting beam current density of 9.3×10^{12} ions per cm^2, yielding a dose rate of 3.2×10^{-6} dpa s^{-1}.

The damage depth profile and displacement damage were calculated using the Stopping and Range of Ions in Matter (SRIM-2013) program using the "Detailed Calculation" mode and the displacements were obtained from the resulting vacancy.txt file. One downside of this software is its inability to model precise nano-structures, so for these calculations a compact layer of TiO_2 (density of 3.89 g cm^{-3}) was used. The displacement energy for titanium and oxygen was set to 25 and 28 eV, respectively. The 200 keV proton flux produces a relatively uniform damage profile through ~1 μm (Fig. 2), which ensured that the entire length of the nanotubes would receive a consistent irradiation dose. Using the "Detailed Calculation" mode the number of displacements per ion-angstrom was 3.6 $\times 10^{-3}$ vacancies per angstrom per ion at the peak implantation depth, which was converted to a fluence of 2.18×10^{17} ions per cm^2 to reach the average accumulated proton dose of 0.17 dpa.

Electrochemical testing

Li half-cells were assembled in coin-type cells (Hohsen 2032) with Li metal foil (FMC Lithium) as the negative electrode, a 2325 type polymer separator, and 1.2 M $LiPF_6$ in ethylene carbonate/ethyl methyl carbonate (3 : 7 weight ratio) electrolyte (Tomiyama). Half-cells were cycled galvanostatically at varying currents between 2.5 and 0.9 V vs. Li/Li^+ using an automated Maccor battery tester at ambient temperature. Three-electrode cells were prepared using ECC-Ref cells (EL-Cell) with Lithium metal as both the counter and reference electrode. GITT and cyclic voltammetry (CV) measurements were carried out in three-electrode cells using a Bio-Logic Science Instruments potentiostat/galvanostat (VMP-300). GITT measurements consisted of a series of current pulses of 8 μA for 30 min and a 2 h rest period until the voltage reached a cut-off value of 1 V. CV measurements for all samples were performed with the potential window of 0.9–2.5 V at the scan rates of 0.5, 1, 2, 5, and 10 mV s^{-1}. All cell assembly and disassembly operations were performed in an Ar-filled glovebox with oxygen levels below 0.5 ppm. The mass of the TiO_2 nanotube films was determined by peeling off the nanotube film from the Ti substrate using adhesive tape and measuring the weight difference. The remaining substrate was examined by SEM to ensure that no residual TiO_2 nanotubes were left on the substrate.

Electron microscopy

Scanning electron microscopy (SEM) images were recorded with a FEI Teneo field emission microscope operating at 5 kV. Transmission electron microscopy (TEM) images, including HRTEM, SAED, and EELS spectra, were recorded with a JEOL JEM-2100F operating at 200 kV and a Gatan GIF Tridiem at Brookhaven National Laboratory.

Raman spectroscopy

Raman spectroscopy was conducted using a Horiba Scientific LabRAM HR Evolution spectrometer using a 442 nm He:Cd laser with signal accumulations of three 30 s scans. After instrument calibration, the samples were scanned at room temperature under ambient conditions. The incident laser power was 100 mW, and samples were viewed at a magnification of 100×. Scattered light was collected with a thermoelectrically cooled Si CCD detector. Data were acquired using LabSpec 6 Spectroscopy Suite software and analyzed using OriginPro software.

Electrical conductivity measurements

Gold pads (2 mm in diameter) were thermally evaporated on top of the masked TiO_2-nanotubes-on-Ti substrates at a grazing angle of 30 degrees to limit the gold-nanowire contact only at the apex of the nanotubes without touching the metal Ti at the bottom, thus to avoid any short circuits. The conductance of different substrates was studied from the current–voltage (I–V) curves measured by connecting the gold pads and Ti substrates using a Gamry reference 600 potentiostat.

Notes

H. Xiong designed all experiments. J. Wharry designed the proton irradiation experiments. K. Smith and A. Savva prepared the electrodes. K. Smith and C. Deng conducted the electrochemical measurements. K. Smith and A. Savva conducted the Raman measurements. S. Hwang and D. Su conducted the TEM measurements and analysis. Y. Wang and K. Smith conducted the proton irradiation experiments. H. Xiong, K. Smith, A. Savva, and D. Cheng analyzed the data. All authors discussed the results and contributed to the manuscript preparation. H. Xiong, K. Smith, C. Deng and J. Wharry wrote the manuscript.

Acknowledgements

References

1 D. Deng, M. G. Kim, J. Y. Lee and J. Cho, *Energy Environ. Sci.*, 2009, **2**, 818–837.
2 Z. G. Yang, D. Choi, S. Kerisit, K. M. Rosso, D. H. Wang, J. Zhang, G. Graff and J. Liu, *J. Power Sources*, 2009, **192**, 588–598.
3 G. N. Zhu, Y. G. Wang and Y. Y. Xia, *Energy Environ. Sci.*, 2012, **5**, 6652–6667.
4 C. D. Joyce, T. McIntyre, S. Simmons, H. LaDuca, J. G. Breitzer, C. M. Lopez, A. N. Jansen and J. T. Vaughey, *J. Power Sources*, 2010, **195**, 2064–2068.
5 B. Zachauchristiansen, K. West, T. Jacobsen and S. Atlung, *Solid State Ionics*, 1988, **28**, 1176–1182.
6 P. G. Bruce, B. Scrosati and J. M. Tarascon, *Angew. Chem., Int. Ed.*, 2008, **47**, 2930–2946.
7 A. S. Arico, P. Bruce, B. Scrosati, J. M. Tarascon and W. Van Schalkwijk, *Nat. Mater.*, 2005, **4**, 366–377.
8 M. Wagemaker, W. J. H. Borghols and F. M. Mulder, *J. Am. Chem. Soc.*, 2007, **129**, 4323–4327.
9 L. Kavan, M. Kalbac, M. Zukalova, I. Exnar, V. Lorenzen, R. Nesper and M. Graetzel, *Chem. Mater.*, 2004, **16**, 477–485.
10 J. Maier, *J. Power Sources*, 2007, **174**, 569–574.
11 Y. Wang and G. Z. Cao, *Adv. Mater.*, 2008, **20**, 2251–2269.
12 A. Manthiram, A. V. Murugan, A. Sarkar and T. Muraliganth, *Energy Environ. Sci.*, 2008, **1**, 621–638.
13 J. S. Chen, Y. L. Tan, C. M. Li, Y. L. Cheah, D. Luan, S. Madhavi, F. Y. C. Boey, L. A. Archer and X. W. Lou, *J. Am. Chem. Soc.*, 2010, **132**, 6124–6130.
14 Y. S. Hu, L. Kienle, Y. G. Guo and J. Maier, *Adv. Mater.*, 2006, **18**, 1421–1426.
15 E. Baudrin, S. Cassaignon, M. Koesch, J. P. Jolivet, L. Dupont and J. M. Tarascon, *Electrochem. Commun.*, 2007, **9**, 337–342.
16 D. H. Wang, D. W. Choi, Z. G. Yang, V. V. Viswanathan, Z. M. Nie, C. M. Wang, Y. J. Song, J. G. Zhang and J. Liu, *Chem. Mater.*, 2008, **20**, 3435–3442.
17 B. P. Hahn, J. W. Long and D. R. Rolison, *Acc. Chem. Res.*, 2013, **46**, 1181–1191.
18 B. Koo, H. Xiong, M. D. Slater, V. B. Prakapenka, M. Baasubramanian, P. Podsiadlo, C. S. Johnson, T. Rajh and E. V. Shevchenko, *Nano Lett.*, 2012, **12**, 2429–2435.
19 B. Koo, S. Chattopadhyay, T. Shibata, V. B. Prakapenka, C. S. Johnson, T. Rajh and E. V. Shevchenko, *Chem. Mater.*, 2013, **25**, 245–252.
20 J. Lee, A. Urban, X. Li, D. Su, G. Hautier and G. Ceder, *Science*, 2014, **343**, 519–522.
21 M. M. Thackeray, S. H. Kang, C. S. Johnson, J. T. Vaughey, R. Benedek and S. A. Hackney, *J. Mater. Chem.*, 2007, **17**, 3112–3125.
22 T. Ohzuku, M. Nagayama, K. Tsuji and K. Ariyoshi, *J. Mater. Chem.*, 2011, **21**, 10179–10188.
23 D. Qian, B. Xu, M. Chi and Y. S. Meng, *Phys. Chem. Chem. Phys.*, 2014, **16**, 14665–14668.

This journal is © The Royal Society of Chemistry 2017

J. Mater. Chem. A, 2017, **5**, 11815–11824 | **11823**

24 H. Xiong, H. Yildirim, E. V. Shevchenko, V. B. Prakapenka, B. Koo, M. D. Slater, M. Balasubramanian, S. K. R. S. Sankaranarayanan, J. P. Greeley, S. Tepavcevic, N. M. Dimitrijevic, P. Podsiadlo, C. S. Johnson and T. Rajh, *J. Phys. Chem. C*, 2012, **116**, 3181–3187.

25 H. Xiong, H. Yildirim, P. Podsiadlo, J. Zhang, V. B. Prakapenka, J. P. Greeley, E. V. Shevchenko, K. K. Zhuravlev, S. Tkachev, S. K. R. S. Sankaranarayanan and T. Rajh, *Phys. Rev. Lett.*, 2013, **110**, 078304.

26 D. R. Rolison and L. F. Nazar, *MRS Bull.*, 2011, **36**, 486–493.

27 H. A. Shukur, M. Sato, I. Nakamura and I. Takano, *Adv. Mater. Sci. Eng.*, 2012, 1–7.

28 L. Z. Qin, B. Liao, X. L. Dong, X. Y. Wu, X. G. Hou and A. D. Liu, *Nucl. Instrum. Methods Phys. Res., Sect. B*, 2009, **267**, 1077–1080.

29 N. Matsunami, M. Uebayashi, K. Hirooka, T. Shimura and M. Tazawa, *Nucl. Instrum. Methods Phys. Res., Sect. B*, 2009, **267**, 1654–1657.

30 R. Fromknecht, I. Khubeis, S. Massing and O. Meyer, *Nucl. Instrum. Methods Phys. Res., Sect. B*, 1999, **147**, 191–201.

31 O. Meyer, I. Khubeis, R. Fromknecht and S. Massing, *Nucl. Instrum. Methods Phys. Res., Sect. B*, 1998, **136**, 436–441.

32 O. Meyer, I. Khubeis, R. Fromknecht and S. Massing, *Nucl. Instrum. Methods Phys. Res., Sect. B*, 1997, **127**, 624–628.

33 S. K. Zheng, T. M. Wang, C. Wang and G. Xiang, *Nucl. Instrum. Methods Phys. Res., Sect. B*, 2002, **187**, 479–484.

34 S. K. Zheng, T. M. Wang, W. C. Hao and R. Shen, *Vacuum*, 2002, **65**, 155–159.

35 D. Su, F. Wang, C. Ma and N. Jiang, *Nano Energy*, 2013, **2**, 343–350.

36 G. S. Was, *Fundamentals of Radiation Materials Science: Metals and Alloys*, Springer, 2007.

37 B. P. Uberuaga and X. M. Bai, *J. Phys.: Condens. Matter*, 2011, **23**, 435004.

38 X. M. Bai and B. P. Uberuaga, *JOM*, 2013, **65**, 360–373.

39 T. Hartmann, L. M. Wang, W. J. Weber, N. Yu, K. E. Sickafus, J. N. Mitchell, C. J. Wetteland, M. A. Nastasi, M. G. Hollander, N. P. Baker, C. R. Evans, J. R. Tesmer and C. J. Maggiore, *Nucl. Instrum. Methods Phys. Res., Sect. B*, 1998, **141**, 398–403.

40 N. Liu, V. Haublein, X. M. Zhou, U. Venkatesan, M. Hartmann, M. Mackovic, T. Nakajima, E. Spiecker, A. Osvet, L. Frey and P. Schmuki, *Nano Lett.*, 2015, **15**, 6815–6820.

41 J. M. Macak, H. Tsuchiya, A. Ghicov, K. Yasuda, R. Hahn, S. Bauer and P. Schmuki, *Curr. Opin. Solid State Mater. Sci.*, 2007, **11**, 3–18.

42 J. F. Ziegler, J. P. Biersack, U. Littmark, *The Stopping Range of Ions in Solids*, Pergamon Press, New York, 1985.

43 E. Silva, F. A. La Porta, M. S. Liu, J. Andres, J. A. Varela and E. Longo, *Dalton Trans.*, 2015, **44**, 3159–3175.

44 P. Tengvall, T. P. Vikinge, I. Lundstrom and B. Liedberg, *J. Colloid Interface Sci.*, 1993, **160**, 10–15.

45 S. Sahoo, A. K. Arora and V. Sridharan, *J. Phys. Chem. C*, 2009, **113**, 16927–16933.

46 Y. Lei, L. D. Zhang and J. C. Fan, *Chem. Phys. Lett.*, 2001, **338**, 231–236.

47 W. B. Hu, L. P. Li, G. S. Li, C. L. Tang and L. Sun, *Cryst. Growth Des.*, 2009, **9**, 3676–3682.

48 V. Swamy, B. C. Muddle and Q. Dai, *Appl. Phys. Lett.*, 2006, **89**, 163118.

49 V. Swamy, A. Kuznetsov, L. S. Dubrovinsky, R. A. Caruso, D. G. Shchukin and B. C. Muddle, *Phys. Rev. B: Condens. Matter Mater. Phys.*, 2005, **71**, 184302.

50 S. P. S. Porto, P. A. Fleury and T. C. Damen, *Phys. Rev.*, 1967, **154**, 522–526.

51 V. Swamy, D. Menzies, B. C. Muddle, A. Kuznetsov, L. S. Dubrovinsky, Q. Dai and V. Dmitriev, *Appl. Phys. Lett.*, 2006, **88**, 243103.

52 K. K. Tiong, P. M. Amirtharaj, F. H. Pollak and D. E. Aspnes, *Appl. Phys. Lett.*, 1984, **44**, 122–124.

53 H. Heusler, J. Epping, S. Heusler, E. Richter, N. P. E. Vermeulen and D. D. Breimer, *J. Chromatogr.*, 1981, **226**, 403–412.

54 J. M. Zhang, M. Lang, R. C. Ewing, R. Devanathan, W. J. Weber and M. Toulemonde, *J. Mater. Res.*, 2010, **25**, 1344–1351.

55 M. Toulemonde, W. J. Weber, G. S. Li, V. Shutthanandan, P. Kluth, T. F. Yang, Y. G. Wang and Y. W. Zhang, *Phys. Rev. B: Condens. Matter Mater. Phys.*, 2011, **83**, 054106.

56 M. Toulemonde, J. M. Constantini, C. Dufour, A. Meftah, E. Paumier and F. Studer, *Nucl. Instrum. Methods Phys. Res., Sect. B*, 1996, **116**, 37–42.

57 J. M. Costantini, F. Brisard, M. Toulemonde and F. Studer, *Nucl. Instrum. Methods Phys. Res., Sect. B*, 1997, **122**, 514–521.

58 A. Tighineanu, *Friedrich-Alexander Universität Erlangen-Nürnberg*, 2014, p. 183.

59 A. Gloter, C. Ewels, P. Umek, D. Arcon and C. Colliex, *Phys. Rev. B: Condens. Matter Mater. Phys.*, 2009, **80**, 035413.

60 Z. Y. Wu, G. Ouvrard, P. Gressier and C. R. Natoli, *Phys. Rev. B: Condens. Matter Mater. Phys.*, 1997, **55**, 10382–10391.

61 G. Bertoni, E. Beyers, J. Verbeeck, M. Mertens, P. Cool, E. F. Vansant and G. Van Tendeloo, *Ultramicroscopy*, 2006, **106**, 630–635.

62 M. Wagemaker, G. J. Kearley, A. A. van Well, H. Mutka and F. M. Mulder, *J. Am. Chem. Soc.*, 2003, **125**, 840–848.

63 M. V. Koudriachova, N. M. Harrison and S. W. de Leeuw, *Phys. Rev. Lett.*, 2001, **86**, 1275–1278.

64 J. Wang, J. Polleux, J. Lim and B. Dunn, *J. Phys. Chem. C*, 2007, **111**, 14925–14931.

65 H. Lindstrom, S. Sodergren, A. Solbrand, H. Rensmo, J. Hjelm, A. Hagfeldt and S. E. Lindquist, *J. Phys. Chem. B*, 1997, **101**, 7717–7722.

66 A. J. Bard and L. R. Faulkner, *Electrochemical Methods: Fundamentals and Applications*, John Weiley & Sons, New York, 1980.

67 V. Augustyn, P. Simon and B. Dunn, *Energy Environ. Sci.*, 2014, **7**, 1597–1614.

68 H. Xiong, M. D. Slater, M. Balasubramanian, C. S. Johnson and T. Rajh, *J. Phys. Chem. Lett.*, 2011, **2**, 2560–2565.

11824 | *J. Mater. Chem. A*, 2017, **5**, 11815–11824

This journal is © The Royal Society of Chemistry 2017